NANOCLUSTERS:

Their Generation and Characterization in Beams and the Bulk

L.H. Kidder, C.A. Fancher, J.M. Collins, H.W. Sarkas, D.W. Robinson, C.A. Jones*, and **K.H. Bowen**, Department of Chemistry, Johns Hopkins University, Baltimore, MD 21218, USA

Clusters are aggregates of atoms or molecules, and they can be formed at any size and from any substance. There are two main purposes for studying clusters; (1) for understanding the evolution of materials properties from the atomic/molecular/microscopic world to that of the bulk/condensed matter/macroscopic world and (2) for exploring the novel properties exhibited by some cluster sizes and thus developing the possibility of applications. The term, nanoclusters, simply refers to large clusters whose dimensions are most conveniently measured in nanometers. An outline of the contents of our presentation is provided by its title. There is a molecular beam part and a bulk materials part, with each of these further divided into sections on generation and charaterization.

Nanoclusters in Beams

We have generated a wide variety of neutral, cationic, and anionic nanoclusters. While several sources have been employed in our lab for this purpose, here we wish to focus primarily on those generated with our inert gas condensation-based cluster ion source. This source results from the union of two existing techniques, inert gas condensation cells for forming large aggregates (pioneered by Y. Petrov) and methods for forming cluster ions by injecting low energy electrons directly into effluent gas streams (developed by both H. Haberland and by our group). This source is shown schematically in Figure 1. In it, the material of interest is first vaporized into a waiting cold bath of helium gas at about 1 Torr. There, the vapor is effectively "tricked" thermodynamically, in that it suddenly finds itself cooled to a relatively low temperature by collisions with the cold helium, making it "want" to condense. Since helium is a poor condensation partner, and there are few cool surfaces nearby, the atoms or molecules of the vapor simply condense on themselves, ie., they aggregate and grow into nanoclusters. In effect, this produces a smoke of ultra-small particles of the material being vaporized. Some of these nanoclusters are entrained in a weak flow of helium as it exits the condensation cell through a small (1 mm diameter) aperture in the front of the source. There, low energy electrons are injected from a hot filament directly into the still high density gas stream. Axial magnetic fields in this region help to maintain the resulting microplasma, and it is from this that cluster ions are extracted and transported as a beam. We often loosely refer to this composite device as the Smoke-Ion Source.

The Smoke-Ion Source has several important attributes. (1) It delivers very high intensities of both ionic and neutral clusters. In some cases, its cluster ion intensities are close to being space-charge limited, and its mass-filtered cluster ion deposition rate even 1.6 m from the source is about 50 A/min. (2) It can handle relatively high temperature materials and thus form clusters composed of their atoms or molecules. (3) This source has a propensity for making rather large clusters. Cluster sizes typically range from $n = 100$ to $n = 2{,}000$, n being the number of atomic or molecular components in a given cluster. It is relatively easy to make even larger sizes, and in some cases clusters much smaler than $n = 100$ can also be generated with this source. (4) This source outputs both neutral and charged nanoclusters of both polarities. (5) The Smoke-Ion Source operates continuously, providing the high average fluxes needed in most applications.

INERT GAS NUCLEATION (SMOKE) ION SOURCE

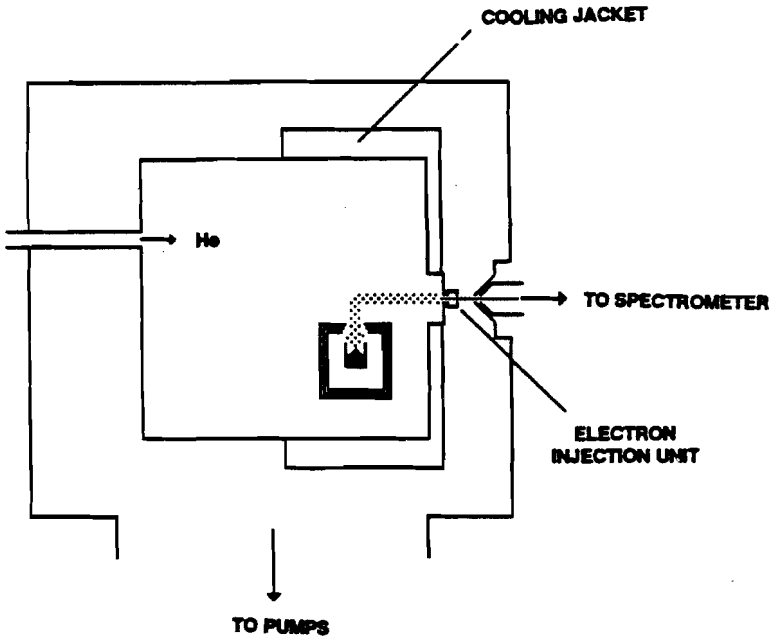

Figure 1

The best way to characterize the performance of this source is to examine mass spectra of its cluster ion output. Most of the mass spectra presented here are those of cluster anions because so much of our work is in cluster anion photodetachment spectroscopy. In order to access the very high mass ranges characteristic of many nanocluster ions, mass resolution has been traded for mass range in the mass spectra presented here, with the result that they appear as unresolved mass spectral envelopes. For example, Figure 2 presents a mass spectrum of vanadium cluster anions. These V_n^- clusters begin to show intensity at n = 180, they display an intensity maximum at n = 330, and their intensity is largely attenuated by n = 570. Figure 3 shows the mass spectrum of $(Cu_2O)_n^-$ cluster anions. Note, that at its peak maximum, n = 45, these are objects having diameters of about 1.5 nm (assuming bulk density). Of greater interest, however, is the narrow size distribution of cluster ions seen here. At its FWHM, it is about 0.2 nm or +5% D,where D is the cluster diameter. Thus, while the variation in mass across the size distribution seen here is substantial, the variation in physical size is rather small. If these cluster were lying on a table, for instance, they would look more like apples and oranges, than basketballs and golf balls. Figures 4-8 show other examples of mass spectra taken with our Smoke-Ion Source. The copper cluster anions in Figure 4 give a higher n_{max} and a broader size distribution than seen in the previous figure. Figure 5 shows the mass spectrum of silver cluster ions, again peaking at a D which is similar to that of the previous two figures. Figure 6 presents the mass spectrum of lithium cluster anions. There, the maximum occurs at D = 3.5 nm and n_{max} = 1,200, and the intensity is very high (for a beam energy of 500 eV). Figure 7 gives a typical mass spectrum of magnesium cluster anions, and Figure 8 provides one more example via tin cluster anions. These are but a few of the nanocluster ion mass spectra that we have taken. Also, we should add that by varying source conditions, the size distributions of such mass spectra can often be changed or shifted substantially.

While recording mass spectra is one approach to characterizing the nanoclusters generated in this source, we would also like to discuss characterization in terms of the optical response of size-selected nanoclusters. As an example of our work in this area, here we will summarize our photoelectron (photodetachment) spectroscopic studies of color centers in negatively-charged cesium iodide nanocrystals. These experiments are conducted by crossing a mass-selected beam of negative cluster ions with a fixed-frequency visible photon beam, and energy analyzing the resultant photodetached electrons (see Figure 9). Cesium iodide cluster anions, $(CsI)_n^-$, were generated in our Smoke-Ion Source by evaporating cesium iodide, and their photoelectron spectra are shown in Figure 10. In each case, these are single broadened peaks which shift with increasing cluster size to successively higher electron binding energies. As shown in Figure 11, the size dependence of our $(CsI)_n^-$ photodetachment threshold energy data is linear with $n^{-1/3}$, which itself is proportional to R^{-1}, where R is the radius of a given cluster. This is consistent with theoretical expectations for this system. The fact that all of our data points fall on the same straight line indicates that they are all related, ie., they are all the same kind of species. The most important aspect, however, is the intercept, since it should correspond to the bulk value of the photodetachment threshold energy, ie., the photoelectric threshold (PET). Extrapolation of our data yields an intercept of 2.2 eV, and this is also the value of the PET for F centers in bulk cesium iodide crystals. Thus, it is clear that the cesium iodide nanocrystals that we examined are indeed embryonic forms of F centers, which are maturing with size toward bulk F centers. While F centers have been seen in small alkali halide clusters before, this is the first time that larger ones have been studied, establishing a clear connection with the bulk. When the source was operated under more violent source conditions, a second set of features appeared in the photoelectron spectra. We believe that these are due to metal-rich cesium iodide cluster anions, $Cs(CsI)_n^-$. Figure 12 shows examples of photoelectron spectra taken during both the tamer, (a), and the more violent, (b), source conditions. The second feature is clearly visible in each of the Figure 12b spectra. Plotting these new features (along with the earlier ones) on a $n^{-1/3}$ plot (see Figure 13)

Mass Spectrum of Vanadium Cluster Anions

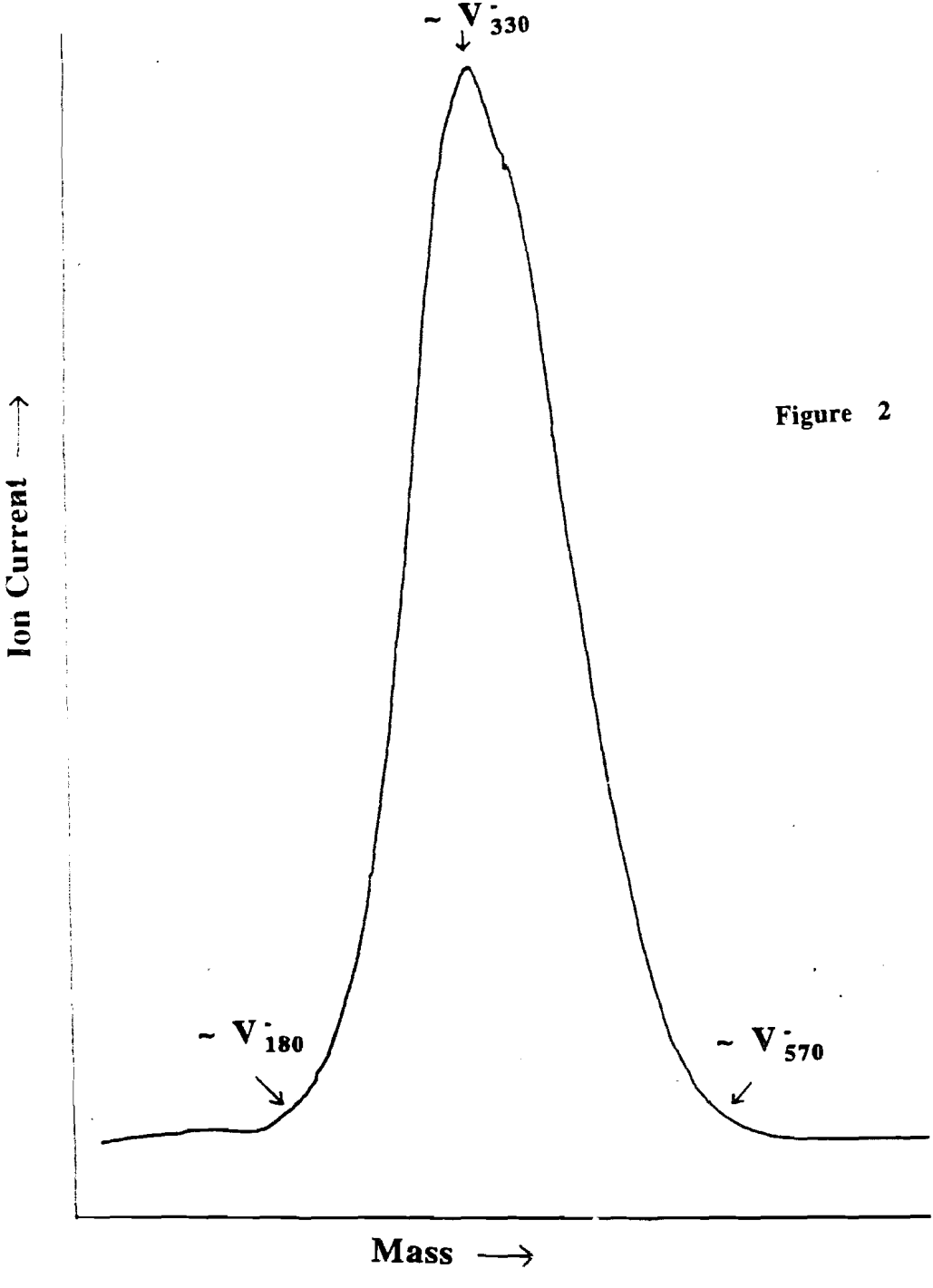

Figure 2

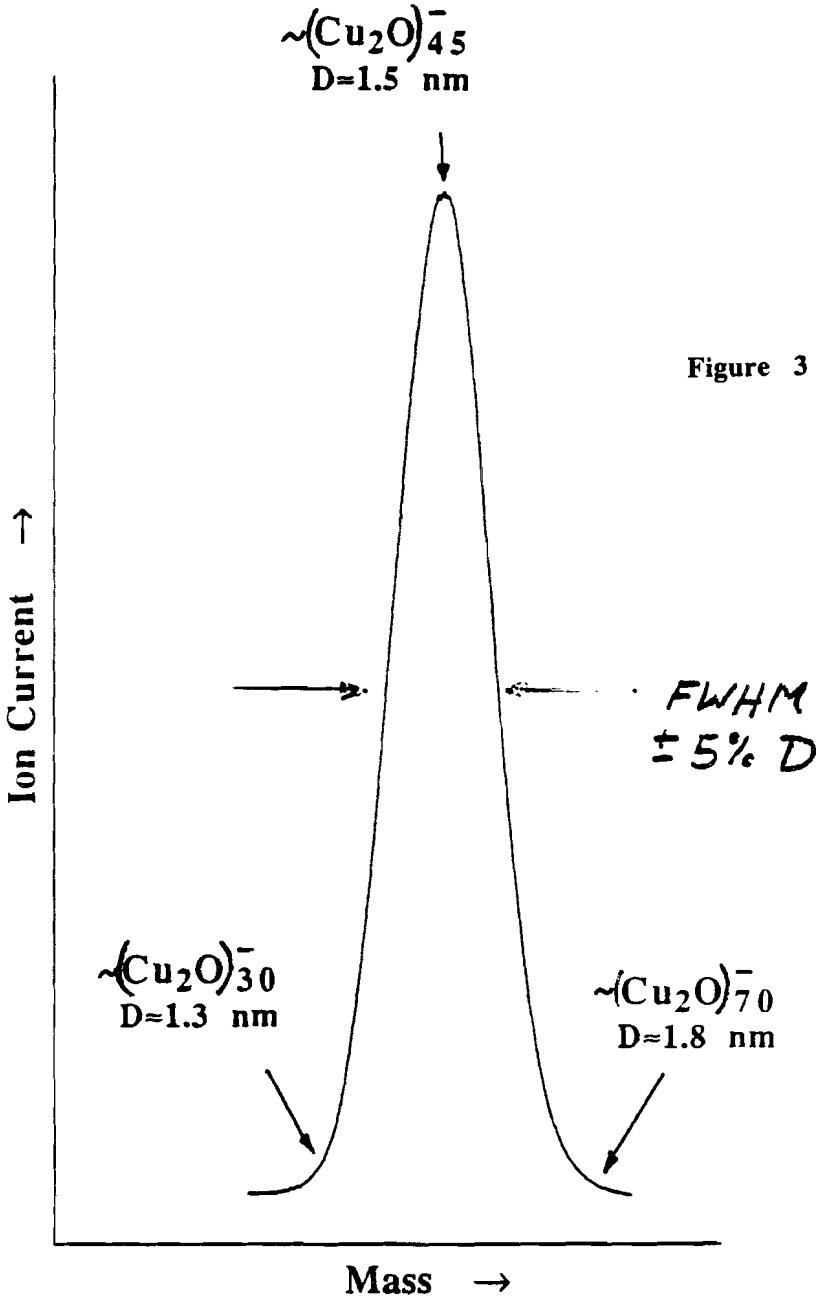
~(Cu2O)-45
D=1.5 nm
Ion Current →
FWHM
± 5% D
~(Cu2O)-30
D=1.3 nm
~(Cu2O)-70
D=1.8 nm
Mass →

Figure 3

Mass Spectrum of Copper Cluster Anions

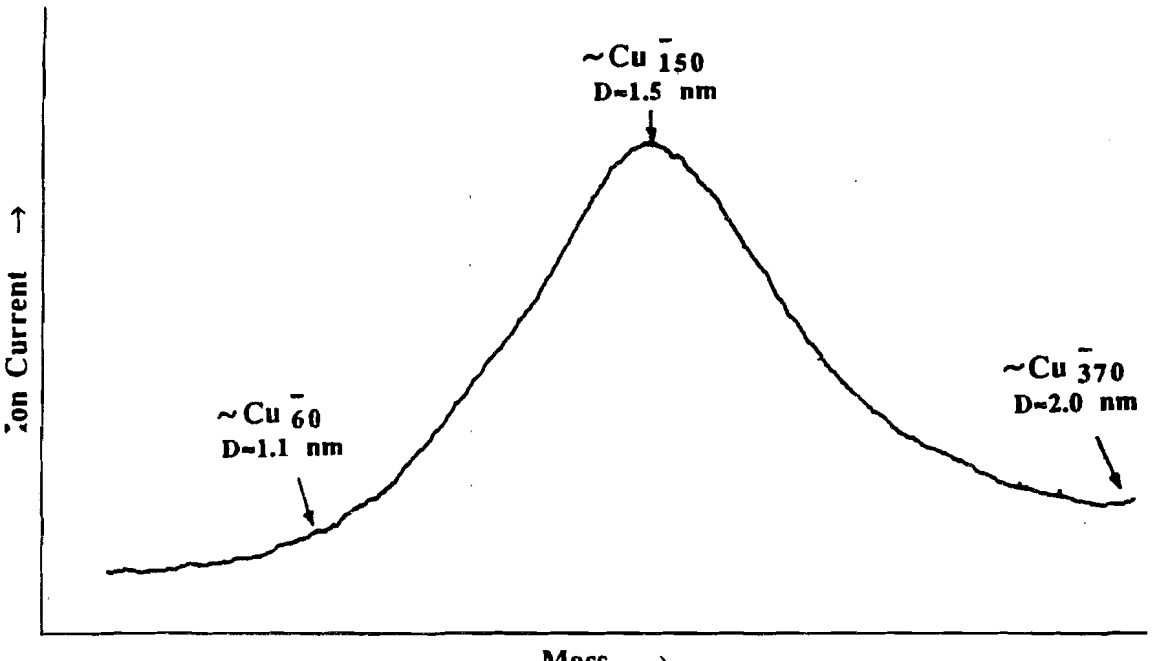

Figure 4

Mass Spectrum of Silver Cluster Anions

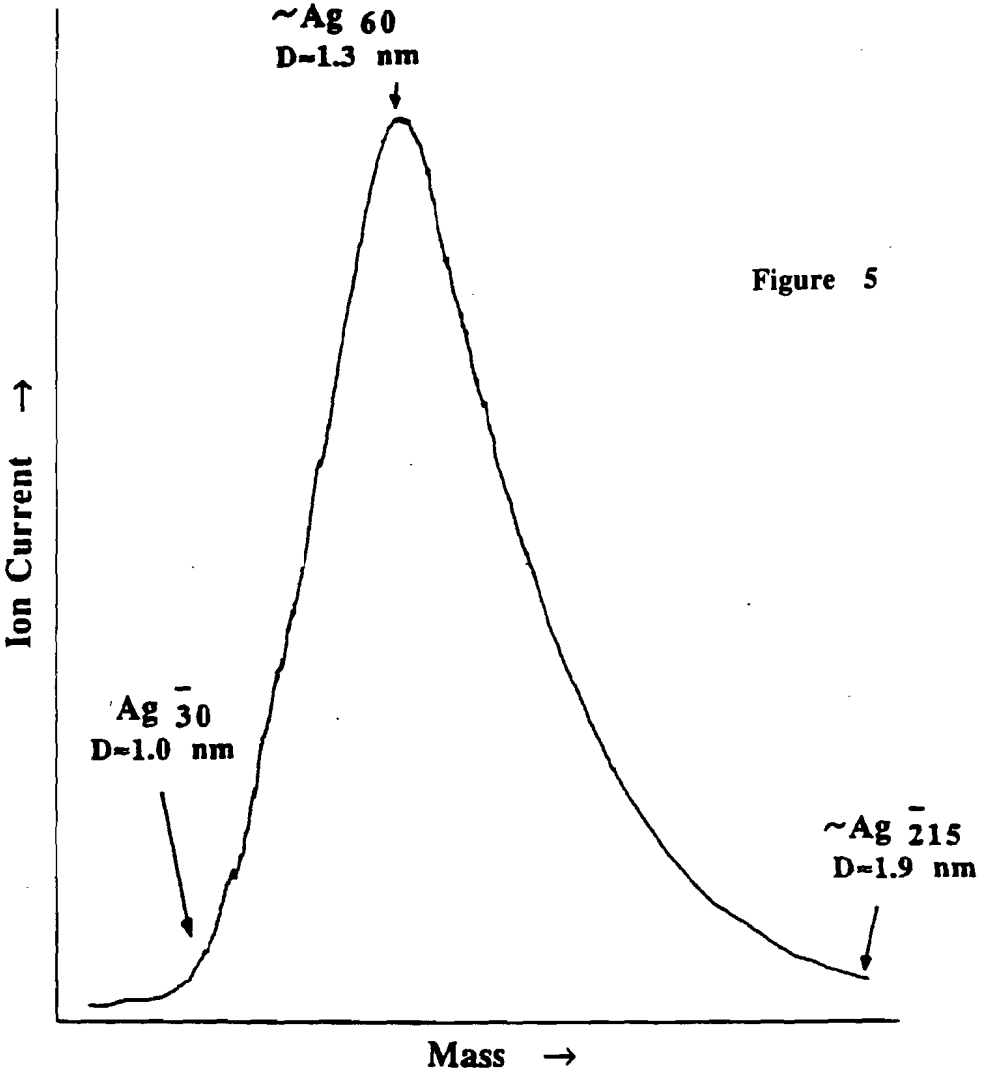

Figure 5

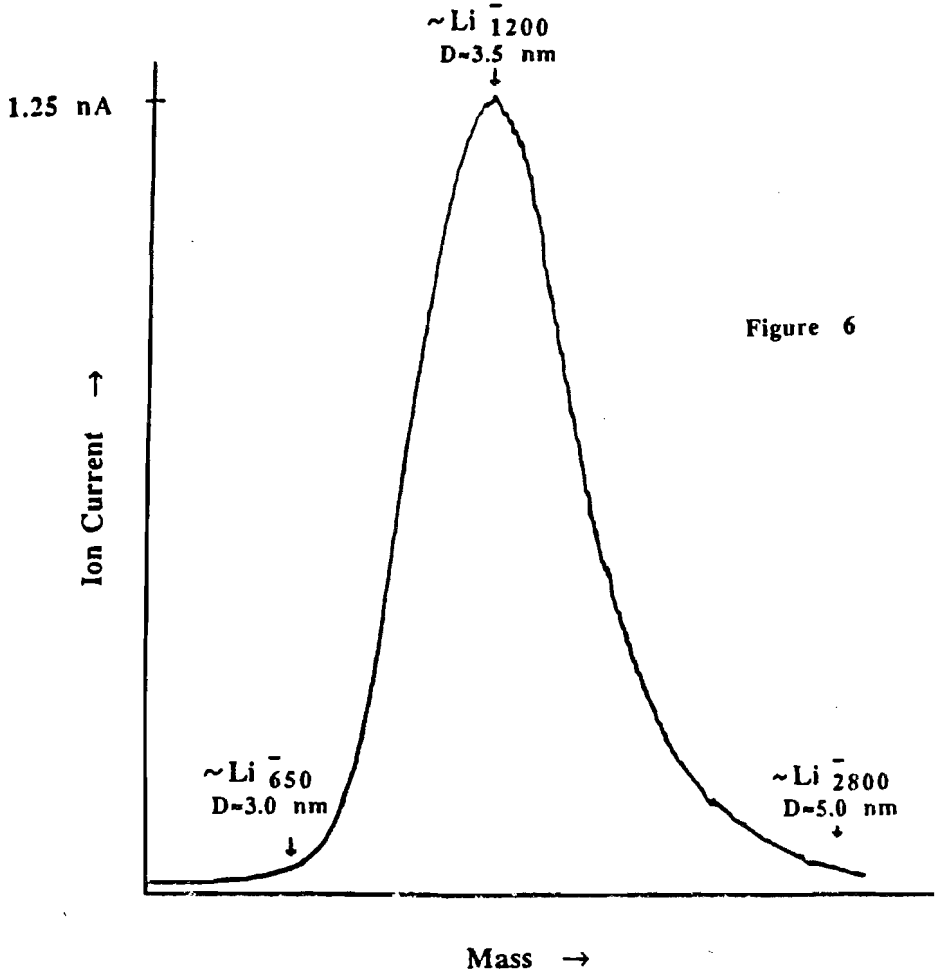
~Li 1200
D=3.5 nm
1.25 nA
Ion Current →
~Li 650
D=3.0 nm
~Li 2800
D=5.0 nm
Mass →

Figure 6

Mass Spectrum of Magnesium Cluster Anions

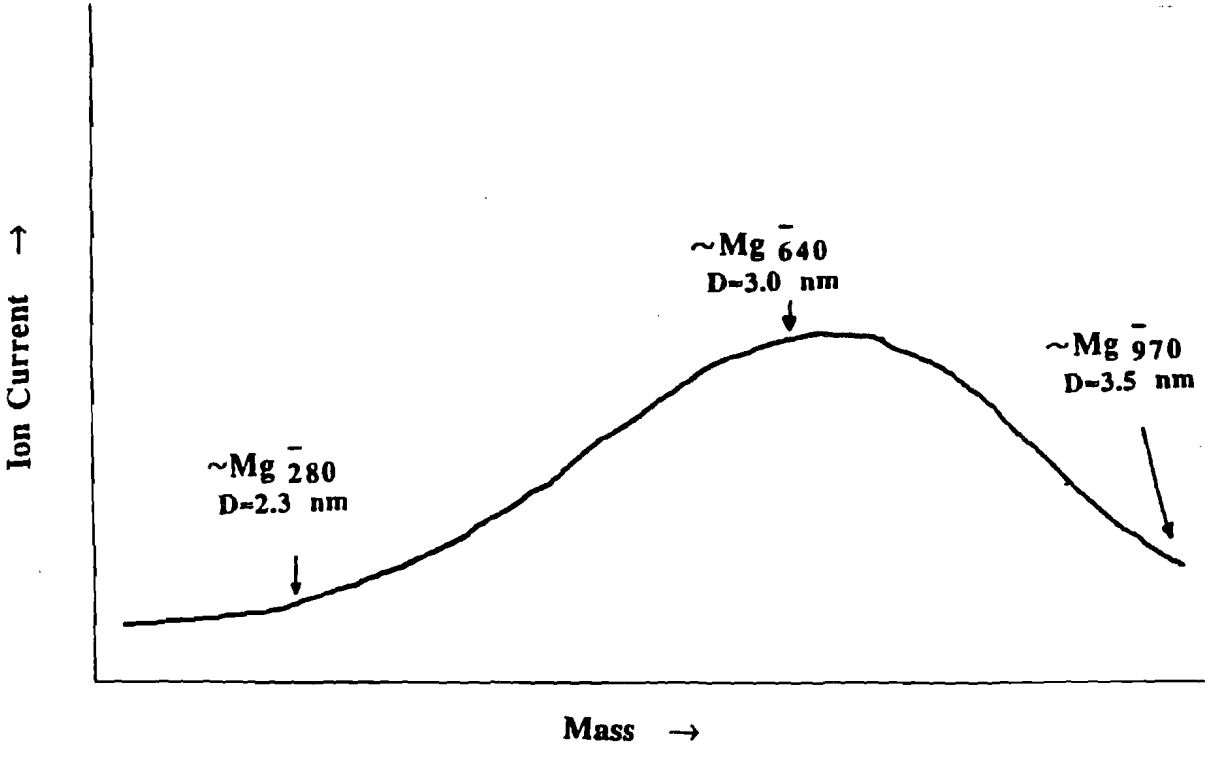

Figure 7

Mass Spectrum of Tin Cluster Anions

Figure 8

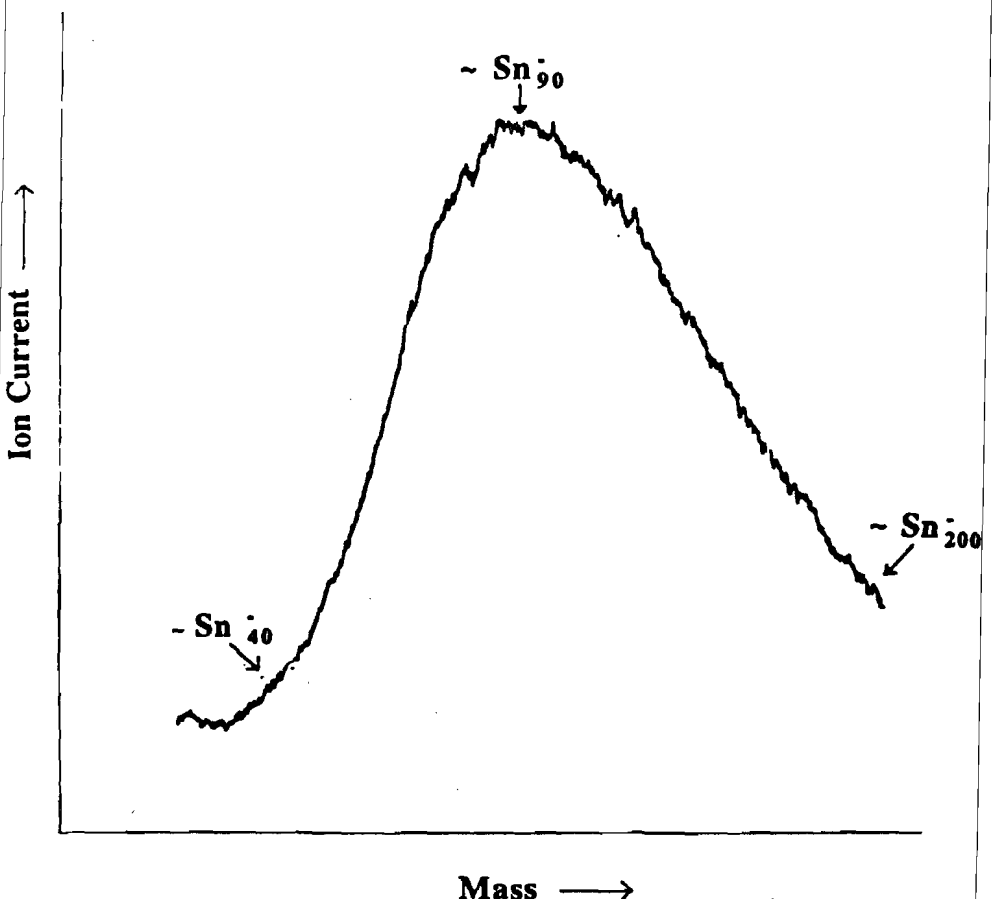

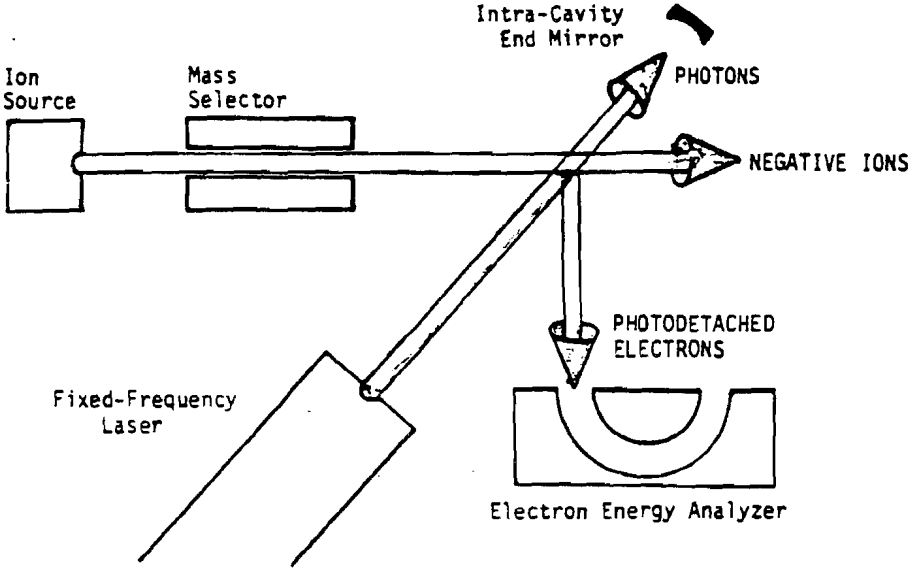
Intra-Cavity
End Mirror
PHOTONS
Ion
Source
Mass
Selector
NEGATIVE IONS
PHOTODETACHED
ELECTRONS
Fixed-Frequency
Laser
Electron Energy Analyzer

Figure 9

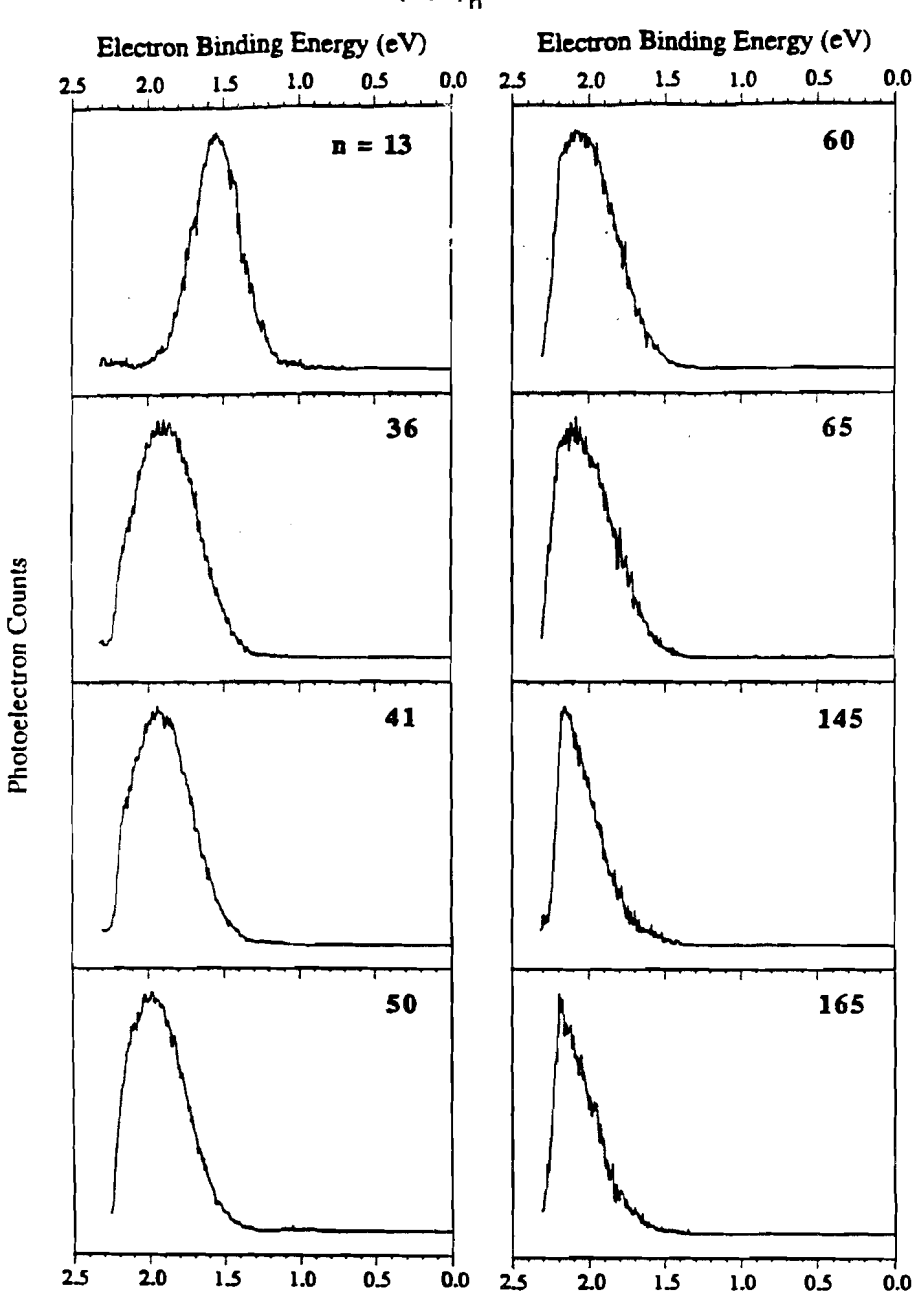
$(CsI)_n^-$
Electron Binding Energy (eV)
Electron Binding Energy (eV)
2.5 2.0 1.5 1.0 0.5 0.0
n = 13
36
41
50
60
65
145
165
Photoelectron Counts

Figure 10

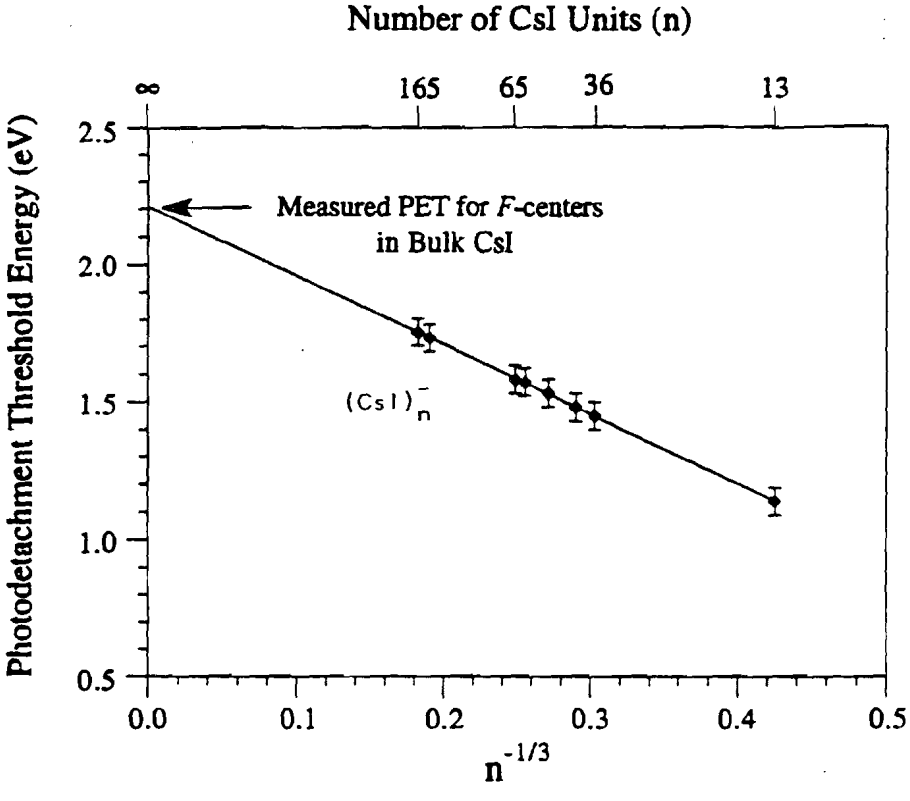
Number of CsI Units (n)
∞
165
65
36
13
Photodetachment Threshold Energy (eV)
2.5
2.0
1.5
1.0
0.5
Measured PET for F-centers
in Bulk CsI
(CsI)n−
0.0
0.1
0.2
0.3
0.4
0.5
n-1/3

Figure 11

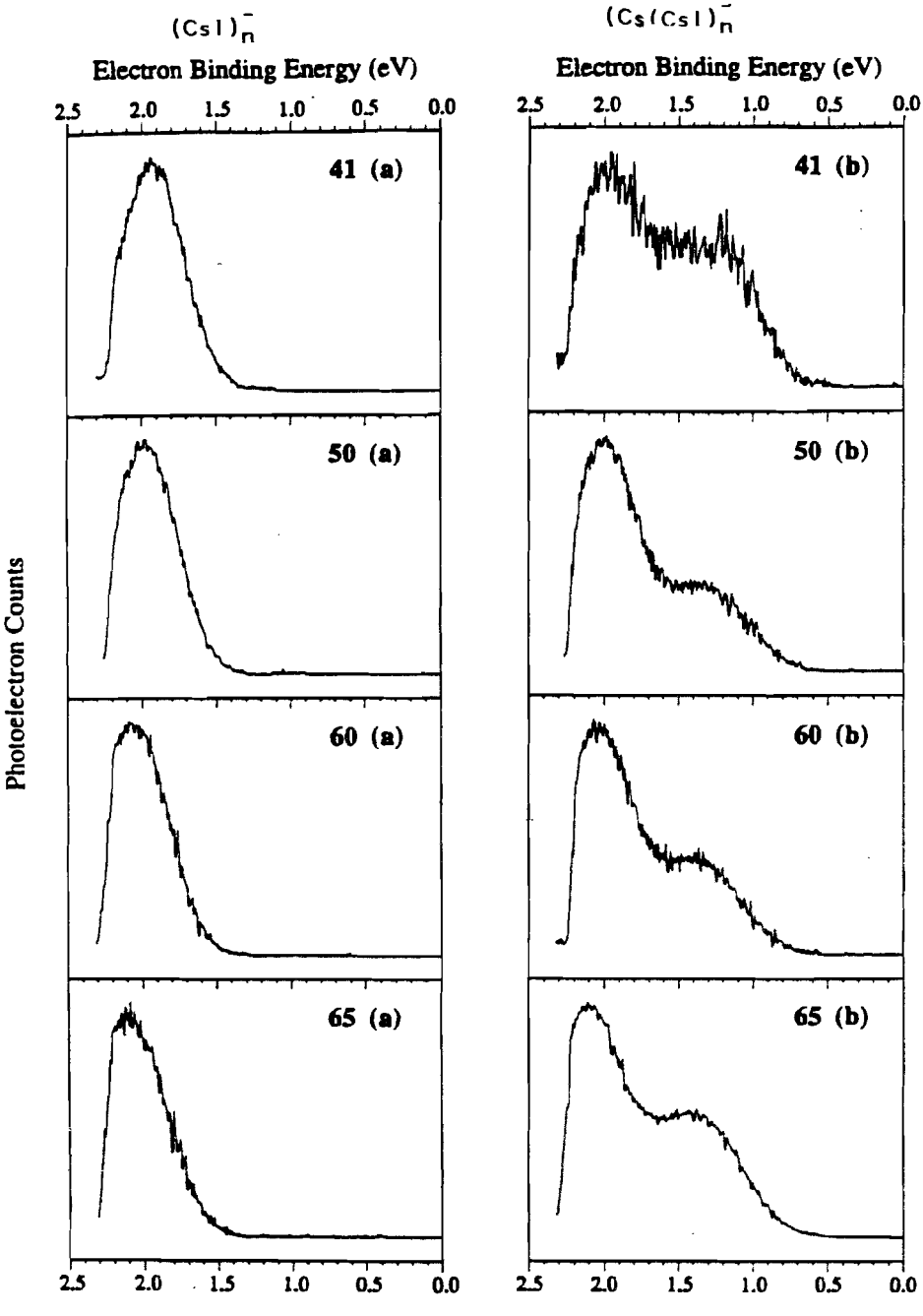
$(CsI)_n^-$
Electron Binding Energy (eV)
2.5 2.0 1.5 1.0 0.5 0.0
41 (a)
50 (a)
60 (a)
65 (a)
$(Cs(CsI)_n^-$
Electron Binding Energy (eV)
2.5 2.0 1.5 1.0 0.5 0.0
41 (b)
50 (b)
60 (b)
65 (b)
Photoelectron Counts

Figure 12

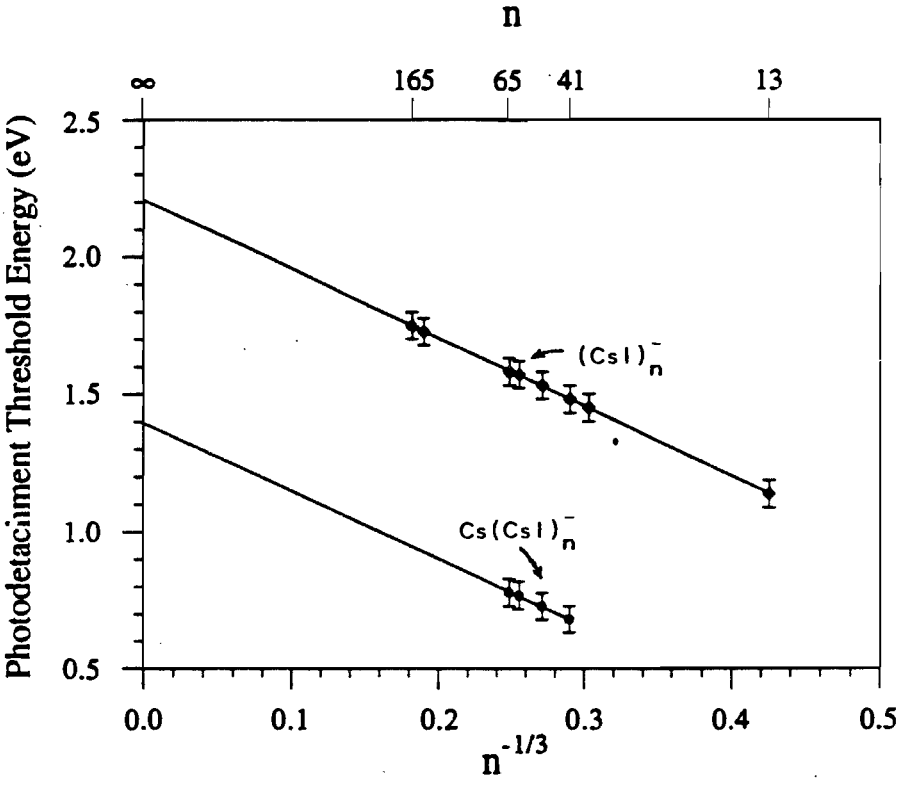
n
∞
165
65
41
13
2.5
2.0
1.5
1.0
0.5
Photodetacıment Threshold Energy (eV)
(CsI)$_n^-$
Cs(CsI)$_n^-$
0.0
0.1
0.2
0.3
0.4
0.5
n$^{-1/3}$

Figure 13

shows that they too give a straight line of similar slope to the earlier plot . Here, however, the intercept is 1.4 eV, close to the expected PET for bulk F' centers in cesium iodide. An F center arises due to the substitution of an electron for an anion in an ionic material. F' centers are less well known, but they arise due to the substitution of two electrons for an anion. In cesium iodide nanocluster anions, we are seeing size effects due to both F and F' centers.

Nanocluster Powders in Bulk

For every substance from which we made nanocluster beams outside of the Smoke-Ion Source, we were simultaneously generating nanocluster powders inside it. These powders, also known as nanophase materials, were simply scraped from inside the source where they had deposited as by-products during operation. Characterization of these powders by TEM revealed nanometer dimensional particles ranging in size from a few nanometers in diameter to several tens of nanometers in lateral dimension. In addition, some of them were well-formed symmetric crystals, including many flat plates and cubes.

Some of our work with nanocluster powders has been motivated by an interest in the potential of these materials as unsupported catalysts. Nanophase materials have several promising catalytic attributes. (1) They possess very high surface areas. Figure 14 illustrates the point. If a 1 micron diameter particle has a surface area of $1 m^2/gm$, then a 1 nm diameter particle has a surface area of 1,000 m^2/gm. (2) Nanoclusters have novel electronic properties. They should therefore have unusual chemical reactivities, some of which may postively affect catalytic activity and perhaps selectivity. (3) Nanopowders largely maintain their nano-domains even when pressed into pellets at moderate pressures. Such samples have very high gas diffusivities. (4) Lastly, nanoparticles can exhibit a high degree of geometric surface defects. Some or all of these properties should be attributes in catalysis. The main disadvantage of nanophase catalysis is the tendency of ultra-small particles to revert to their thermodynamically most stable bulk states. This tendency depends largely on the temperature, the pressure, the particle size, and of course the nature of the specific substance. Our strategy has been to choose a class of substances that are, in both bulk and nano-states, relatively resistant to sintering and/or melting. This led us to metal oxide nanoclusters, and our interest in nanophase catalysis (and chemical sensors) has led us further to mixed metal oxide nanoclusters.

With our collaborator, C.A. Jones at ARCO Chemical Company, we undertook a set of preliminary experiments to see if the nanophase material form of a known bulk catalyst would offer any advantages. For a variety of practical reasons (the main one being that we had to evaporate two metals from a single multi-compartment crucible with a target composition ratio in mind), we focused on lithium magnesium oxide. Lithum promoted magnesium oxide, known as the Lunsford catalyst, is used primarily for the partial oxidation of methane (see Figure 15). At the usual working temperature of the bulk catalyst, the nanopowder form of LiMgO was clearly different, and it showed an increase in cataytic acticity by a factor of about five over that of the bulk catalyst. We had hoped for a somewhat greater increase due to its greater surface area. When we examined the sample by SEM, however, the reason was evident; there had been substantial sintering into larger particles. Lithium no doubt has a propensity to do this, and catalysts with little or no alkali metal in them would probably be more resistant to sintering. It was at lower temperatures, however, that we were pleasantly surprised. There, the nanopowder form of LiMgO showed threshold catalytic activity fully 200 C **below** the temperature at which threshold catalytic activity appears in the bulk Lunsford catalyst! This is a stiking result of substantial importance if it holds up as being general in other systems. It means that there may be useful nanoparticle properties that appear in temperature ranges well below those where sintering becomes a problem.

Generating nanoparticles inside our Smoke-Ion Source has an advantage and a disadvantage.. The advantage is that one can sample, via the nanocluster ion beam and mass spectrometry, what is

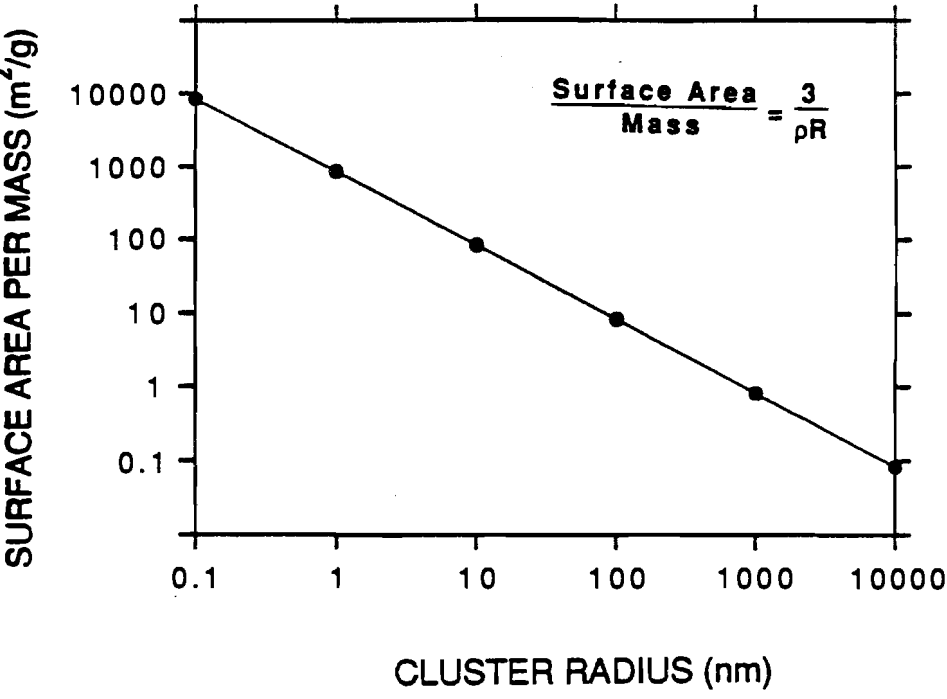
SURFACE AREA PER MASS (m^2/g)
10000
1000
100
10
1
0.1
Surface Area / Mass = 3 / ρR
0.1
1
10
100
1000
10000
CLUSTER RADIUS (nm)

Figure 14

Lithium Promoted Magnesium Oxide
(The Lunsford Catalyst)

$CH_4 + O_2 \longrightarrow$ Ethylene, Ethane, Higher Hydrocarbons
Water, Carbon Monoxide, Carbon Dioxide, Hydrogen

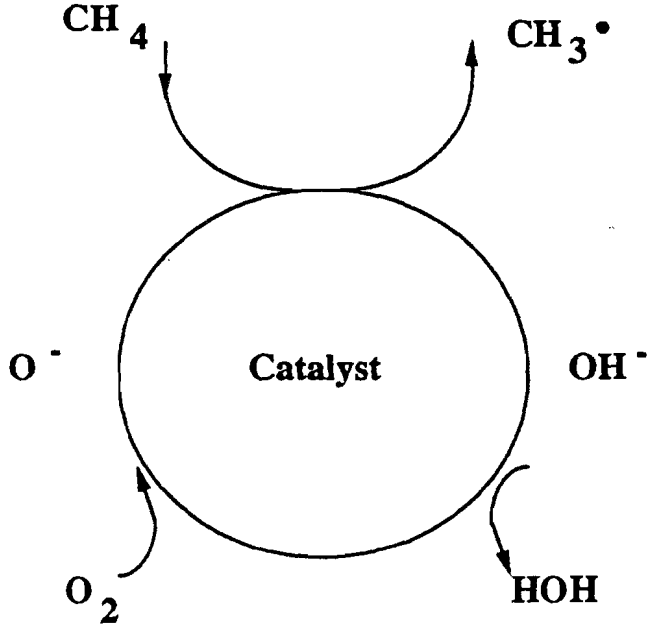

The Rate-Limiting Step is :

$$O^-_{surf} + CH_4 \longrightarrow OH^-_{surf} + CH_3^\bullet$$

For an Effective Catalyst:

(1) High Surface Area is Desired

(2) A "Rough" Surface is Desired

Figure 15

happening inside the source while it is taking place, thus providing an opportunity for steering the source conditions toward those that make the size distribution and/or composition of choice. The disadvantage is the lack of space inside this source, making it difficult to install additional crucibles or other vaporization devices. Recall that this source was originally designed primarily to be an ion source, not a nanoparticle generator.

To rectify this problem, we recently constructed a larger nanophase material generator with plenty of room for multiple and/or alternate vaporization devices. This new generator is shown schematically in Figure 16. It has two side-by-side stations for thermal crucibles, an adjustable cold trap for nanoparticle collection, viewports, pumping ports (one of which is connected to a 4 inch diffusion pump), and ports for a magnetron, for an electron beam, and for a laser beam. It was first tested by evaporating titanium to form titanium nanoparticles. These were post-oxidized on the cold trap with pure oxygen. This produced a brillant flash and generated TiO_2 nanoparticles. Our approach for the present is to make mixed metal nanoparticles with this new generator and post-oxidize them on the cold trap once it is warmed up. For control of composition we want two separate sources, one for each metal. The problem to overcome is how to mix the two metals while they are still in atomic vapor form, ie., before they aggregate significantly, so that they aggregate as a mixture. During the first month of this generator's operation, we have employed two methods for doing this. Both involve evaporating the two metals in very close proximity to one another, so that one is being evaporated in the hot region of the other. These two appraoches are shown in Figure 17. In one appraoch two thermal evaporators are placed close to one another. This is achieved by wraping one of the metals, in the form of a wire, around a tungsten filament heater and locating it just above a boat containing the other metal. We will abbreviate this as the T,T method. The other appraoch that we have used thus far uses a thermal source for one metal and laser vaporization for evaporizing the other metal, abbreviated here as the L,T method. We have used green light from a YAG laser for this purpose. Laser vaporization has two advantages here; (1) it can vaporize refractory materials with relative ease, and (2) vaporization can be made to occur in the mouth of the other crucible, thus insuring the spatial proximity that we seek. Examples of systems that we have recently begun to examine are; Ag*/Al by the T,T method, Ag*/Al by the L,T method, Cu/Cr (1:1) by the T,T method, Pt*/Al by the L,T method, Pt*/Fe by the L,T method, Pd*/Al by the T,T method, and Ag*/Y by the T,T method. The symbol, *, indicates the minority component in each case. All of these mixed metal nanoparticle samples were post-oxidized as described above, and all of them have counterparts among known bulk catalysts. Our work with these and related systems is continuing.

Acknowledgements: This work was supported partly by the National Science Foundation under grant # CHE-9007445 and partly by ARCO Chemical Company.

* Dr. C.A. Jones is with the ARCO Chemical Company, Newtown Square, PA

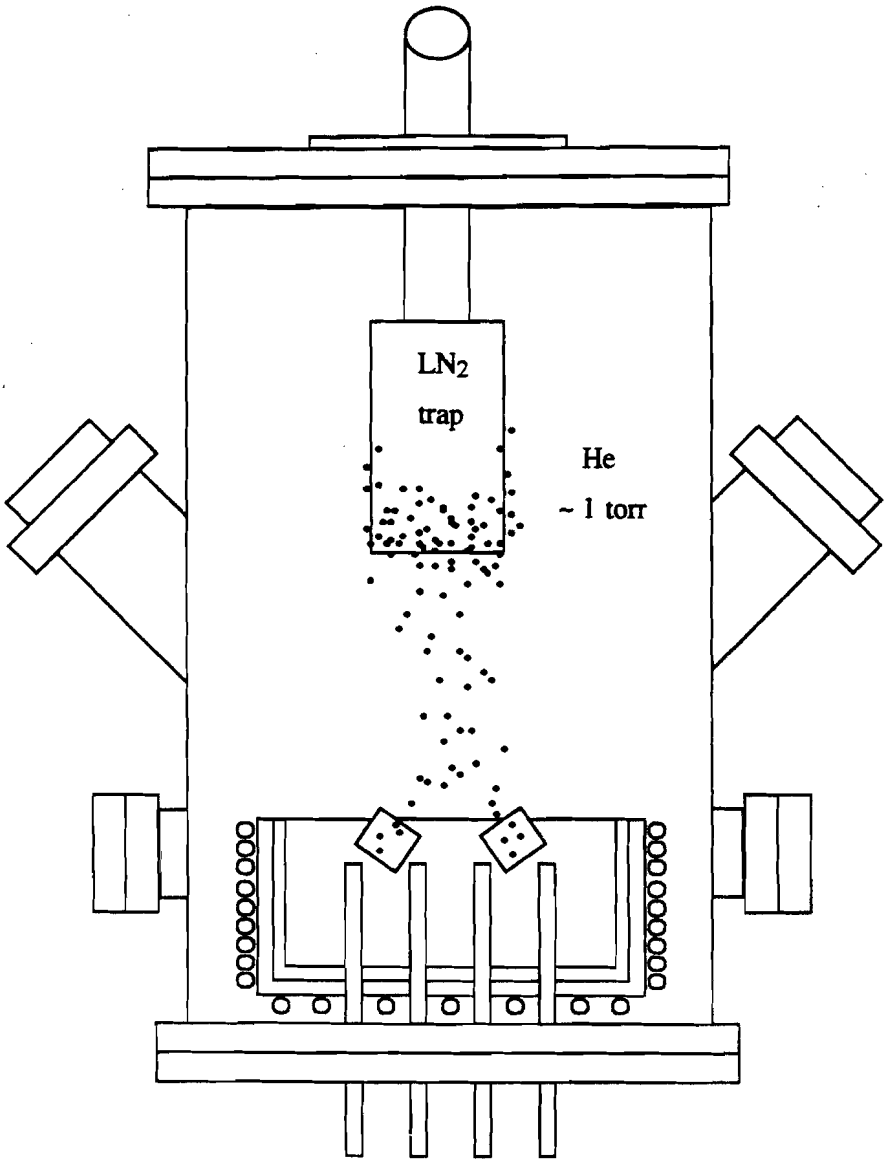

INERT GAS CONDENSATION NANOPHASE POWDER GENERATOR

Figure 16

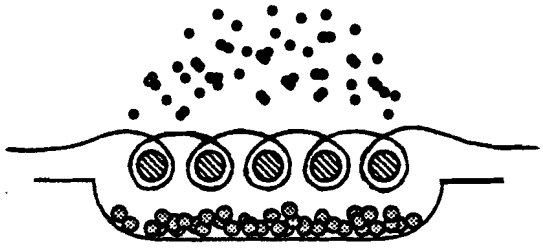

TWO THERMAL EVAPORATORS

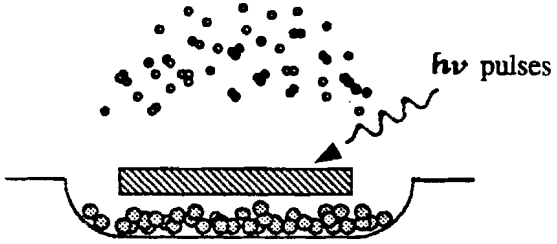

ONE THERMAL AND ONE LASER EVAPORATOR

Figure 17